Multiscale modeling for food drying: A Downscaling approach

Zachary G. Welsh[a], Vindya Thathsaranee Weligama Thuppahige[a,b] and M. A. Karim*[a]

[a] Mechanical, Medical and Process Engineering, Queensland University of Technology, Brisbane, Australia

[b] Department of Food Science and Technology, Faculty of Agriculture, University of Ruhuna, Mapalana, Kamburupitiya, 81100, Sri Lanka

Corresponding author: Azharul Karim, Queensland University of Technology

2 George Street, QLD 4000 Australia, azharul.karim@qut.edu.au

ABSTRACT

Modeling cellular-level transport phenomena in plant-based food materials during drying remains a complex challenge. Intracellular water (ICW) plays a critical role in drying kinetics but is often overlooked in computational models. Multiscale modeling offers a potential approach to capture the effects of ICW; however, existing models frequently neglect ICW dynamics or predetermine its transport. This work aims to develop a multiscale downscaling model which can actively downscale a materials condition (dependent variables) to investigate the transport of ICW. Two different drying temperatures (47°C and 64°C) and the ICW transport at three different points of interest within the domain are investigated. The results were compared to experimental data and a control model. The downscaling model predicts drying at 47°C very well achieving mean relative errors (MREs) of 3.62% and 0.66% for the average moisture content and average temperature respectively. At 64°C, the model also predicts drying well achieving MREs of 8.38% and 0.90% for the average moisture content

and average temperature respectively. The ICW at each point of interest was calculated and its trend through the cell wall revealed interesting findings.

Keywords: multiscale modeling, cell rupturing, food drying, downscaling

NOMENCLATURE

Abbreviations	
FW	Free water
ICW	Intracellular water
REV	Representative elementary volume
Symbol	
a	Constant
C	Macroscale instantaneous moisture concentration (mol m^{-3})
c	Microscale concentration (mol m^{-3})
c_p	Specific heat of apple tissue (J kg^{-1} K^{-1})
$c_{p\ air}$	Specific heat of air (kJ kg^{-1} K^{-1}**)**
D	Cellular diffusivity (m^2 s^{-1})
$D_{H,eff}$	Upscaled effective moisture diffusivity (m^2 s^{-1})
D_{FW}	Diffusivity of free water (m^2 s^{-1})
D_{ICW}	Diffusivity of intracellular water (m^2 s^{-1})
h_{fg}	Latent heat of evaporation (J kg^{-1})
h_m	Mass transfer coefficient (m s^{-1})
h_T	Heat transfer coefficient (W m^{-2} K^{-1})
k	Thermal conductivity of apple tissue (W m^{-1} K^{-1})
k_c	Gordon and Taylor constant
L_c	Characteristic length (m)

M_{db}	Moisture content dry basis (kg kg^{-1} dry basis)
M_{db}	Dry basis moisture content (kg kg^{-1} dry basis)
$\overline{M}_{db,num}$	Average predicted moisture content (kg kg^{-1} dry basis)
M_w	Molar mass of water (kg mol^{-1})
n	Unit vector normal to the boundary
P_m	Permeability of the cell wall (m s^{-1})
$p_{v\,air}$	Vapor air pressure of ambient air (Pa)
$p_{v\,eq}$	Equilibrium vapor pressure (Pa)
$p_{v\,sat}$	Saturated vapor pressure of water (Pa)
q_c	Mass flux (mol m^{-2} s^{-1})
R	Universal gas constant (J mol^{-1} K^{-1})
t	Time (s)
T_{air}	Drying air temperature (K)
T_{cell}	Temperature of the cell (K)
T_g	Glass transition temperature
T_{g0}	Initial glass transition temperature
T_{gw}	Glass transition temperature of water
T	Temperature (K)
u_1 and u_2	Corrective factors
v	Air velocity (m s^{-1})
v_n	Shrinkage velocity (m s^{-1})
X	Distance (m)
WC_{ICW}	Intracellular water content
β	Coefficients

ψ	Point of interest
ρ	Density of apple tissue (kg m^{-3})
ω	Area of the macroscale domain (m^2)

1. INTRODUCTION

Plant-based food materials (PBFMs) have heterogeneous cellular structures comprising of three main cellular environments with each environment containing water of different characteristics: free water (FW) in intercellular spaces, intracellular water (ICW) in intracellular spaces and strongly bound water within the cell walls (Khan et al., 2018), Figure 1. Drying PBFMs involves simultaneous heat and multiphase mass transfer which dynamically changes a material in terms of its properties, characteristics and final quality (Weligama Thuppahige et al., 2024). These changes originate within the heterogeneous cellular structure of the material and propagate across multiple length scales (cellular/microscale to tissue/macroscale). These changes are a direct result of the complex internal water migration during drying, specifically the transport of ICW is a major concern during drying due to its influence on materials cellular structure. However, the transport of ICW is complex as it depends on the spatial and temporal drying conditions in addition to the property changes the material is experiencing (Welsh et al., 2023). ICW can transport two main ways, apoplastic transport where ICW migrates from intracellular spaces to intercellular spaces after a cell membrane ruptures or through symplastic transport where ICW migrates from cell to cell via fine capillaries (Weligama Thuppahige et al., 2024). The use of computational mathematical models to understand and control the effects of migrating ICW is essential in designing optimal drying processes. However, ICW and its effects are rarely considered in mathematical models of food drying.

[Figure 1 can be placed here]

Whitaker (1977) theory forms the foundation for many modern mathematical models. The theory derives a mechanistic macroscale model using the concept of a representative elementary volume (REV) considering the microscale heat, mass and momentum conservation equations of each phase (solid, liquid water, water vapor and air). However, Whitaker theory fails to consider the material's heterogeneity and assumes no ICW exists, rather it assumes all water is located outside the solid matrix. This often results in the Whitaker model performing better in the early stages of drying. To overcome and compensate for this oversimplistic assumption, condition dependent properties are embedded within the computational models. Condition dependent properties (i.e. diffusivity) are properties which are accurate only when modeling the specific scenario/conditions in which the property was originally derived, for example properties which depend on a specific material, drying conditions (i.e. air temperature, air speed) and/or the dryer configuration. Additionally, the further the simulated conditions deviate from the original conditions in which the property was derived, the less accurate the property becomes. One approach which can aid in transitioning away from condition-dependent properties while considering ICW is multiscale modeling. Multiscale modeling considers a series of sub-models over multiple length scales, giving it the ability to incorporate large amount of physics for a reasonable computational cost (Welsh et al., 2018). There are two main types of multiscale models, one way coupled models and two-way coupled (concurrent) models (Welsh et al., 2018). A one way coupled multiscale model transfers information in one direction, either through upscaling or downscaling. In such models, properties are often computed considering the structure of the particular material and upscaled to inform a larger scale. Alternatively, dependent variables can be downscaled to analyze the behavior at a smaller scale. Concurrent or two way coupled models, on the other hand, allow bidirectional

information exchange. Here, data flows back and forth between scales, with each scale evolving simultaneously and influencing the other. This concurrent exchange includes upscaling, downscaling, and mutual information exchange throughout the simulation, enabling both scales to adjust based on the other's evolving state (Welsh et al., 2018). Multiscale modeling has gained recent attention in the field of food drying modeling with various multiscale models being developed based on various assumptions. Qiu et al. (2022) developed a pore scale multiscale model for impingement drying of a porous slab. The work demonstrated the strength of predicting the drying performance through their multiscale approach to transport properties rather than the traditional condition dependent approach. Tan et al. (2023) also developed a pore-scale model for the heat-moisture and stress-stain distributions for high-moisture porous media. However, these works failed to consider ICW as all water considered was located in the pores/capillaries rather than the solid material.

Over the years there has been a few cellular models and multiscale models which have considered ICW within the solid material. Fanta et al. (2013) developed a microscale model to better understand the underlying phenomena of pear dehydrating under isothermal conditions at 25 ºC. The work considered water in each cellular environment, allowing the work to investigate the different pathways water can flow. The largest gradients in water content were observed across the cell walls and cell membranes. Rahman et al. (2018) also developed a micro-level transport model for drying apple parenchyma cells while considering ICW and conducting an in-depth sensitivity investigation. Prawiranto et al. (2018) constructed a cellular 3D continuum model for the dehydration of apple. The study considered water in various cellular environments and modelled dehydration with a predetermined set of cellular changes/conditions (turgid, free shrinkage, lysis and plasmolysis). However, these works developed only cellular models rather than multiscale models, utilizing a single microscale domain to represent the transport occurring and often modelled predetermined

conditions/scenarios for deformation and/or relative humidity. During drying, significant spatial and temporal variations (in terms of moisture and temperature) develop within a product which cannot be fully understood/investigated with a singular microscale domain. These variations are especially evidence in the later stages of drying when the inner portion of the material can be fully wet/saturated, whereas the outer cells of the material can be fully dried and deformed. Recently, Welsh et al. (2021a) developed a multiscale model for predicting the diffusivity of apple through upscaling during convective drying. The work considered ICW coupled with predetermined temperature dependent domains. The authors later extended their multiscale approach to inversely calculate the temporal cellular diffusivity of ICW in apples (Welsh et al., 2021b) and to construct a generalized diffusivity tensor which is applicable to multiple materials and conditions (Welsh et al., 2023). However, again their work focused on multiscale models which upscaled properties by utilizing predetermined microscale domains and/or considered every possible microscale scenario rather than predicting the spatiotemporal conditions occurring throughout the material. To predict the spatiotemporal conditions the cellular structure is experiencing a multiscale model which is capable of downscaling is required.

This work aims to develop a multiscale model capable of downscaling the dependent variables to appropriately predict the spatiotemporal conditions a material's cellular structure experiences during drying. The work investigates two different drying temperatures (47°C and 64°C) and focuses on the microscales at three different points of interest within the domain. Additionally, the trend of ICW and its flux through the cell wall is investigated. The downscaling approach also incorporated cellular shrinkage through the shrinkage velocity approach paired with X-ray Micro-Computed Tomography (X-ray μCT) data to future improve the generalizability of the multiscale model. The modeling results are also compared to experimental data and a single scale control model.

2. Model Development

2.1 Drying model

A preliminary multiscale model was previously developed considering two spatial scales, a microscale and a macroscale (Welsh et al., 2021a), Figure 2. However, the previous model was only capable of upscaling information, specifically diffusivity, using predetermined conditions at the microscale. This study extends the preliminary model, allowing the model to downscale the required variables and evolve the microscale with time to investigate the different spatiotemporal conditions the cellular structure experiences throughout the entire material. Additionally, the ICW content required to calculate the diffusivity [Equation (16)], is calculated from the size of the intracellular space, outlined in 2.2.6, which is unique to this study. The modeling methods will present the multiscale governing equations, boundary conditions, properties, structure representation at each scale, computational approach, and temporal coupling. The modeling domains for both scales can be found in Figure 2. Additionally, the three points of interest, point 1 (P1), point 2 (P2) and point 3 (P3) are evenly distributed horizontally across the center of the macroscale [denoted by the red dots Figure 2 (a)].

[Figure 2 can be placed here]

2.2 Structure Representation at each scale

The macroscale can be considered as homogeneous following the common approach in literature, however, careful consideration needs to be taken when it comes to the microscale. Two common cellular structure definitions/classifications exist in the literature, (1) macroscopically connected and (2) disconnected inclusions, each effecting the model's assumptions and physics. Over the years, Perré (2019) has considered timber as connected

inclusions for their multiscale models, resulting in an additional “secondary flux” of the divergence of the microscopic flux being considered in the macroscale governing equations when completing the scaling (Perré, 2007, 2019). Karunasena et al. (2015) considered the food material as hexagon shaped cells evolving the porosity through removing some cells from the arrangement for their meshfree models. The resulting structure appears to be disconnected inclusions, though the work does not scale any results. Prawiranto et al. (2018) investigated the transport and cellular changes of a single cuboctahedron shaped apple cell during drying. The cell was located in the center of their 3D domain with voids (or pores) in all eight corners of the cube, however, only basic volume averaging was considered to interpolate the results to the macroscale. Fanta et al. (2014) and Rahman et al. (2018) considered an arrangement of multiple intracellular and intercellular spaces while modeling the transport within the cellular structure of PBFMs. The resulting structure is considered disconnected inclusions, though these works also considered cell walls within the domains. Additionally, these works only model the microscale transport phenomena and no scaling was conducted. In reality, fresh PBFMs generally contain disconnected inclusions (pores) and during drying the structure evolves and if cell rupturing occurs the inclusions will become connected. As a result, the model will consider the structure as connected inclusions, however, as the model is being applied to convective drying, internal convective flow can be neglected and the “secondary flux’ representing the flow through the cell structure is not considered. Nevertheless, if the multiscale approach was applied to model other drying techniques (such as microwave drying) the secondary flux would need to be considered.

The size of the microscale is important due to its effect on computational cost and possible influence on the results. Additionally, the microscale must accurately represent the dynamic microstructure, specifically the domain must represent the two key characteristics which dynamically change during drying, namely the porosity and free/bound water.

Prawiranto et al. (2020) consider multiple domain sizes for dehydrating apple concluding 0.5mm cubed to be sufficient to accurately represent the structure. Carr et al. (2013) developed a multiscale model for timber utilizing a microscale size of 50 µm with two sub-domains, a cell and its cell wall. With this in mind, the microscale domain has a size of 250 µm with an initial cell size of 215 µm calculated from the obtained X-ray µCT images, visually displayed in Figure 2.

2.2.1 Macroscale conservation equations

In an axisymmetric coordinate system, the macroscale transport model was developed with the following assumptions: (1) internal convective flow and heat generation are negligible, (2) drying air properties remain constant, (3) heating is axisymmetric, (4) moisture evaporates solely from the surface, and (5) thermal equilibrium is maintained across all phases. The macroscale mass and energy conservation equations are derived using Fick's law of diffusion and Fourier's law of heat transfer. These equations determine the moisture concentration C (mol/m³) and temperature T (K) as functions of position and time. The respective equations are as follows (Golestani et al., 2013).

$$\frac{\partial C}{\partial t}+\frac{1}{r}\frac{\partial}{\partial r}\left[-D_{H,eff}\, r\, \frac{\partial C}{\partial r}\right]+\frac{\partial}{\partial z}\left[-D_{H,eff}\, \frac{\partial C}{\partial z}\right]=0 \ , \tag{1}$$

$$\rho c_p \frac{\partial T}{\partial t}+\frac{1}{r}\frac{\partial}{\partial r}\left[-k\, r\, \frac{\partial T}{\partial r}\right]+\frac{\partial}{\partial z}\left[-k\, \frac{\partial T}{\partial z}\right]=0 \ , \tag{2}$$

where t is the time (s), ρ represents the density of the food tissue (kg/m^3), c_p is the specific heat of the food tissue (J/(kg·K)), k denotes the thermal conductivity of the food material (W/(m·K)) and $D_{H,eff}$ is the upscaled effective moisture diffusivity (m^2/s). The effective moisture diffusivity varies with temperature and WC_{ICW}, the ICW content (%).

2.2.2 Boundary conditions

The macroscale boundary conditions for the mass flux and heat transfer at the exterior surface was given by,

$$\mathbf{n}\cdot\left[-D_{H,eff}\nabla C\right]=h_m\frac{(p_{v\,eq}-p_{v\,air})}{RT}, \tag{3}$$

$$\mathbf{n}\cdot\left[-k\nabla T\right]=h_T(T-T_{air})-h_m\frac{(p_{v\,eq}-p_{v\,air})}{RT}h_{fg}M_w, \tag{4}$$

where h_m is the mass transfer coefficient (m/s), h_T is the heat transfer coefficient (W/(m^2·K)), $p_{v\,eq}$ is the equilibrium vapor pressure, $p_{v\,air}$ is the vapor air pressure of ambient air (Pa) , **n** is the unit vector normal to the boundary, R is the universal gas constant (J/(mol·K)), T_{air} is the drying air temperature (K), M_w molar mass of water (g/mol) and h_{fg} is the latent heat of evaporation (J/kg). The equilibrium vapor pressure for apple can be determined from the sorption isotherm. Thus, the equilibrium vapor pressure for apple ($p_{v\,eq}$) is (Ratti et al., 1989),

$$p_{v\,eq}=p_{v\,sat}(T)\exp(-0.182M_{db}^{-0.696}+0.232e^{-43.949M_{db}}M_{db}^{0.0411}\ln\left[p_{v\,sat}(T)\right]). \tag{5}$$

where M_{db} is the dry basis moisture content (kg/kg dry basis) (calculated through Equation A.1 in the supplementary material). The saturated vapor pressure is given by (Vega-Mercado et al., 2001),

$$p_{v\,sat}=\exp\left[-\frac{5800.2206}{T}+1.3915-0.0486T+0.4176\times10^{-4}T^2-0.1445\times10^{-7}T^3+6.546\ln(T)\right]. \tag{6}$$

The last boundary condition for the macroscale is the symmetric condition applied at r=0 (Figure 2), defined as

$$\mathbf{n}\cdot\left[-D_{H,eff}\nabla C\right]=0, \tag{7}$$

$$\mathbf{n}\cdot\left[-k\nabla T\right]=0. \tag{8}$$

2.2.3 Microscale mass conservation

To develop the multiscale model, a microscale was defined at each point within the macroscale to represent the heterogeneous structure of the food. This approach is valid when the scale parameter approaches zero, causing the heterogeneities to vanish and resulting in a homogeneous material (Pavliotis & Stuart, 2008; Welsh et al., 2021a). This assumption is crucial for deriving a model through homogenization and is often referred to as the separation of scales (Auriault et al., 2010; Carr & Turner, 2014). The microscale considered two sub-domains, ICW denoted as ω_{ICW} and intercellular water [free water (FW)] denote as ω_{FW}, Figure 2 (b). The macroscale mass transport, Equation (1), is coupled to the microscale mass transport equation defined as,

$$\frac{\partial c}{\partial t}+\frac{\partial}{\partial x}\left(-D\frac{\partial c}{\partial x}\right)+\frac{\partial}{\partial y}\left(-D\frac{\partial c}{\partial y}\right)=0\ , \tag{9}$$

where c is the microscale concentration (mol/m^3) and D is the cellular diffusivity (m^2/s) equaling D_{ICW} if x,y $\in$ ω_{ICW} and D_{FW} if x,y $\in$ ω_{FW}.

2.2.4 Microscale boundary conditions

The coupling between the macroscale and microscale variables occurs at the boundary of the microscale given by,

$$c_{micro}(a,y)=c_{micro}(0,y)+a\frac{\partial C_{\psi}}{\partial r},\qquad 0<y<b \tag{10}$$

$$c_{micro}(x,b)=c_{micro}(x,0)+b\frac{\partial C_{\psi}}{\partial z},\qquad 0<x<a \tag{11}$$

where a and b are the size of the microscale domain and ψ is the point of interest. The fluxes at the boundaries are also coupled through,

$$\begin{aligned} q_c(0,y)\cdot\mathbf{n} &= q_c(a,y)\cdot\mathbf{n}, \qquad 0<y<b \\ q_c(x,o)\cdot\mathbf{n} &= q_c(x,b)\cdot\mathbf{n}. \qquad 0<x<a \end{aligned} \tag{12}$$

The boundary condition for the cell wall is

$$\mathbf{n}\cdot\left[-D_{H,eff}\nabla C\right] = P_m(c-C), \tag{13}$$

where P_m is the permeability of the cell wall. The permeability of the cell wall does have some uncertainty as the thickness of the cell wall changes during drying (Joardder et al., 2015) and as such is investigated in a sensitivity investigation.

2.2.5 Macroscale and microscale diffusivity

To complete the multiscale model the diffusivity for the macroscale and cellular subdomains is required. The ICW diffusivity is (Welsh et al., 2021b),

$$D_{ICW} = \exp\left[-110.32 + 0.55536T_{cell} + 0.095148WC_{ICW} - 0.00090738T_{cell}^2 - 0.0007235WC_{ICW}^2\right], \tag{14}$$

where T_{cell} is the cell temperature (K) and WC_{ICW} is the intracellular water content (mass %). The diffusivity of FW is (Pace, 1962),

$$D_{FW} = 2.26\times10^{-5}\left[\frac{T}{273.15}\right]^{1.81}. \tag{15}$$

The model does not actively upscale the cellular properties to form the macroscale diffusivity, rather the previously developed homogenized diffusivity is utilized (Welsh et al., 2021a). The function for the macroscale diffusivity is (Welsh et al., 2023),

$$D_{H,eff} = \exp\left[-106.6 + 0.5548T_{cell} + 0.029502WC_{ICW} - 0.00090648T_{cell}^2 - 0.00041019WC_{ICW}^2\right]. \quad (16)$$

2.2.6 Evolution of intracellular water- rupturing threshold

The ICW diffusivity function [Equation (14)] incorporates all three transport modes (Welsh et al., 2023), cell to cell, cell to pore and transport through cell rupturing. Therefore, cell rupturing must be incorporated within the evolution of the ICW. Welsh et al. (2023) introduced a rupturing threshold, exploiting the macroscale equilibrium vapor pressure to determine if and when cell rupturing occurs within the material. The model calculated the equilibrium vapor pressure at each point within the domain and once the average macroscale equilibrium vapor pressure of the domain reaches the threshold, cells will begin to rupture. The threshold was inversely calculated by evaluating the maximum average equilibrium vapor pressure when the domain was dried at 50°C, aligning with published experimental results (Halder et al., 2011; Khan et al., 2018). However, once the threshold was reached, Welsh et al. (2023) work utilized time dependent functions for ICW which require sophisticated microscale experimental techniques (such as nuclear magnetic resonance). This significantly limits the approaches applicability to other studies as these techniques are costly and not commonly available. As the current multiscale downscaling model includes an evolving microscale, the evolution of ICW can now be determined directly from the microscale. Therefore, when the cell is at its full size (215µm), the material is at its maximum ICW water content, 87.8% for apple (Khan et al., 2016). Once the cell rupturing threshold is reached the ICW is determined considering the change in cell size. The threshold of apple is considered as 7080 Pa for apple (Welsh et al., 2023).

2.2.7 *Intracellular deformation*

A shrinkage velocity approach was utilized to approximate the shrinkage of macroscale domain and the intracellular space given by (Tuly et al., 2023),

$$\frac{\partial X}{\partial t} \cdot \mathbf{n} = v_n \ , \tag{17}$$

where v_n is the shrinkage velocity (m/s) and $\partial X/\partial t$ is the change in distance over time. The shrinkage velocity for the macroscale domain was calculated by,

$$v_n = a \cdot \frac{(T - T_g)}{(T_0 - T_{g0})} \tag{18}$$

where a is a constant inversely calculated from considering the average shrinkage velocity from the experimental data and the term $(T\text{-}T_g)/(T_0\text{-}T_{g0})$ represents the solid structure mobility factor. This factor characterizes the physical state transition (rubbery/glassy) while providing valuable insights into the correlation between the shrinkage kinetics and structural mobility (Tuly et al., 2025). The glass transition temperature (T_g) can be calculated from the Gordon and Taylor equation given by (Joardder & Karim, 2019; Tuly et al., 2025),

$$T_g = \frac{(1 - MC_{wb})T_{gs} + k_c MC_{wb} T_{gw}}{1 + MC_{wb}(k_c - 1)} \tag{19}$$

where T_g and T_{gs} are the glass transition temperature of binary mixture and dry matter at 47°C and 64°C respectively, T_{gw} is the glass transition temperature of water and k_c represents the Gordon and Taylor constant.

2.2.8 *Other input parameters*

The remaining input parameters are presented in Table 1.

[Table 1 can be placed here]

2.2.9 Mass transfer coefficient

The mass transfer coefficient is a parameter that varies with system conditions, heavily affected by the airflow pattern and the deformation undergone by the product (Defraeye & Radu, 2018). Khan et al. (2020) examined how spatial variations in heat and mass transfer coefficients impact drying behaviour, showing that neglecting airflow distribution can lead to substantial overestimations. To reduce the effect of this variability on the results, the mass transfer coefficient will instead be estimated using an inverse modeling approach. In the inverse problem approach, the mass transfer coefficient (h_m) is treated as an unknown and is estimated by minimizing the discrepancy between simulated and experimental moisture drying curves. To achieve this, the Levenberg-Marquardt optimization algorithm was integrated with the finite element method, using the moisture data as the basis for the objective functions.

$$OF(h_m) = \int \left[\overline{M}_{db,\exp}(t) - \overline{M}_{db,num}(t, h_m) \right]^2 dt, \tag{20}$$

where $\overline{M}_{db,\exp}$ is the average dry basis moisture content from the experimental investigation and $\overline{M}_{db,num}$ is the average dry basis moisture content from the simulation.

2.3 Simulation Methodology

The simulation procedure is outlined in Figure 3. The multiscale mathematical model was solved in LiveLink for MATLAB, a software package which combines COMSOL Multiphysics Simulations with MATLAB programming. Once the macroscale and microscale domains, governing equations, boundary conditions, properties and input parameters were defined, the model could be run from a MATLAB script file. To solve the multiscale model, the macroscale was first simulated for a single timestep, and the macroscale results were extracted. Then the required data was downscaled to the microscale and the microscale was simulated over its own timestep. Then, the extracted macroscale data was imported for the next

timestep, and the procedure is repeated until the drying is complete. Lastly, a sensitivity investigation was conducted.

[Figure 3 can be placed here]

2.3.1 Macro-micro temporal coupling

The temporal coupling is extremely important to consider in a multiscale model and various approaches for temporal coupling exist (Welsh et al., 2018). The current model utilizes a Multigrid/heterogeneous multiscale method (HMM) approach, as shown in Figure 4, where the microscale is not continuously simulated. Microscale simulation was conducted as different timesteps (Figure 3) and key data is downscaled at the exchange timesteps. The downscaling model has a macroscale timestep of 60 seconds, a micro timestep of 0.1 seconds and an exchange timestep of 600 seconds. Additionally, the macroscale is simulated for 21600 seconds and 23400 seconds for drying at 47°C and 64°C respectively and the microscale is simulated for 5 seconds after each exchange step.

[Figure 4 can be placed here]

2.4 Experimental Investigations

Two separate experimental investigations were conducted, the macroscale drying experiments and X-ray μCT. The macroscale drying experiments were conducted to produce validation data to validate the output from the multiscale model whereas the X-ray μCT was conducted to investigate the evolution of the material's microstructure.

2.4.1 Macroscale drying experiments

Granny Smith apples at commercial maturity were purchased from a local supermarket and prepared following the standard sample preparation procedure (Asabe & Home). The

samples were washed and then cut into cylindrical shapes using a stainless-steel Cork Borer (JH-1225). Each sample consisted of the mesocarp (pulp) portion, initially measuring 30 mm in length and 18 mm in diameter. Convective drying was performed at two selected temperatures within the typical air temperature range for drying (40–80 ºC): 47 ºC and 64 ºC, representing different levels of cellular deformation and ICW transport mechanisms. The dryer maintained an air velocity of 1 m/s and the airflow was perpendicular to the sample along the x-y plane. A visual diagram of the dryer can be seen in Figure B.1 in the supplementary material. Model validation was conducted using two data sets: average moisture content and average surface temperature of the samples. To measure moisture content, each sample was weighed individually at regular intervals. This occurred every 10 minutes during the first hour, then every 30 minutes until the drying process was completed. The samples were weighed using a digital balance with a 50 g capacity and ±0.001 g accuracy, with the measuring procedure being completed within 10 seconds (from removal to replacing the sample). A FLIR-E6390 thermal imaging camera was used to record surface temperature. This experimental procedure was repeated three times. The detailed drying experimental procedure and some of the results on the average macroscale moisture content and average surface temperature can be found in the authors' previous publication (Welsh et al., 2023).

2.4.2 X-ray µCT Experiment

In order to extract the cellular deformation of dried apple cells, both the fresh and convective dried (both at 45 °C and 60 °C) cylindrical-shaped Granny Smith apple samples were scanned using an X-ray µCT scanner (µCT50, Scanco Medical, Switzerland). Apple samples were packed in foam and horizontally placed in scanning tubes with a diameter of 34mm. The native resolution, electric potential, current and the power used for these scans were as 10.3 μm^3, 55 kvp, 145 µA, and 8 W, respectively with an average sample scanning

time of 1000 ms and an Aluminum filter (0.1 mm). The scans were carried out in triplicates. Once the scans were completed, the image stacks were exported as DIACOM files into Mimics (Version 24.0, Materialise NV, Belgium) for segmentation using semi-automated thresholding. The consistency of the segmentations was ensured by maintaining a constant threshold value. It should be noted due to the study requirements and equipment limitations the X-ray µCT experimentation was conducted on cylindrical samples with a height of 15 mm and a diameter of 8mm drying at an average temperature of 45°C and 60°C.

3. Results

The results are presented in six main sections, the cellular deformation, the macroscale mass transfer coefficient, the macroscale drying kinetics, the macroscale temperature evolution, the ICW results and a sensitivity investigation. Three points of interest within the macroscale domain, (P1, P2 and P3) were selected along the center of the domain to analyze the model and approach, visually shown in Figure 2. These points were selected as examples to demonstrate how the microscales vary spatially depending on their location in the macroscale. Additionally, the points move in relation to the shrinkage occurring. The multiscale downscaling model was compared to the experimental data and the single scale macroscale model without deformation as a control (Welsh et al., 2023). All properties and heat and mass transfer coefficients were the same for the control and downscaling model.

3.1 Cellular deformation

X-ray µCT was utilized to extract the cellular deformation information of granny smith apple dried at 45°C and 60°C. The quantitative values of the intracellular and pore space (surrounded by at least two or more cells) were extracted from the segmented scanned images using the in-built functions available in MIMICS software. Accordingly, 30 intracellular spaces

and pore spaces were randomly selected across the top, middle and bottom slices of each scanned image. The boundaries of the selected intracellular and pore spaces were defined, and $L^{\perp}$; the minimal diameter orthogonal to the maximum length (L max) values have been extracted and performed in triplicates for higher accuracy. The mean average values for the extracted intracellular and pore sizes were statistically analyzed by performing one-way analysis of variance (ANOVA) at $\alpha = 0.05$, followed by the Turkey's test as the mean separation method using Minitab 18 (Minitab, version 18.1, Minitab LLC, Australia. Evaluating 30 intracellular spaces resulted in average sizes of 215.4 ± 30 µm for fresh apple cells, 128.15 ± 10 µm for dried apple cells using convective air at 45 °C to a moisture content of 0.8 kg/kg dry basis, and 119.10 ± 10 µm for dried apple cells using convective air at 60 °C to a moisture content of 1.23 kg/kg dry basis, (Figure 5). This resulted in condition dependent velocities of -25×10^{-9} m/s and -30×10^{-9} m/s for drying at 47°C and apple dried 64°C respectively. It should be noted, the shrinkage velocity also had to consider the multiscale temporal coupling into its calculation due to the skipped portions of time.

[Figure 5 can be placed here]

3.2 Macroscale mass transfer coefficient

The downscaling model considered a deforming macroscale domain. Furthermore, the control model (Welsh et al., 2023) simulated drying without macroscale deformation. This resulted in unique mass transfer coefficients for each scenario, a mass transfer coefficient of 0.00699 m/s when simulating drying with deformation compared to 0.00381 m/s for the control model (Welsh et al., 2023). The uncovered values were used for the remainder of the study. During drying, the mass transfer coefficient depends on the velocity field (spatially dependent) and macroscale deformation (temporal dependent) (Khan et al., 2020). When simulating drying without deformation like the control model, the mass transfer coefficient is significantly lower to compensate for the missing physics (deformation) and a non-spatially dependent mass

transfer coefficient. When drying is simulated with deformation, the mass transfer coefficient is much closer to the real scenario as the inverse study only has to compensate for the constant mass transfer coefficient.

3.3 Macroscale - Drying Kinetics

The downscaling model accurately predicted the moisture transport at 47°C achieving a mean relative error (MRE) of 3.62% when compared to the experimental results (Welsh et al., 2023), Figure 6. The control model (Welsh et al., 2023) achieved a similarly low MRE of 1.52%. The multiscale downscaling model slightly underpredict the experimental data in the middle stages of drying, 50-250 mins. In the later stage, the model slightly overpredicts the transport, demonstrating a trend opposite to that of the control. This is likely due to the inclusion of deformation in the downscaling model, whereas deformation was not considered in the control. The downscaling model and control model resulted in almost identical diffusivities between 1.94×10^{-10} and 2.16×10^{-10} m^2/s for drying at 47°C, Figure 7. At 64°C the downscaling model predicted the moisture transport accurately achieving a MRE of 8.38% when compared to the experimental results, Figure 6. The control macroscale model achieved a similarly low MRE of 4.80%, predicting the experimental data slightly better. The multiscale downscaling model slightly underpredict the experimental data between 35-150 mins for drying at 64°C and then slightly overpredicted the experimental data in the later stages, following the same trend as predicting drying at 47°C. When drying at 64°C, the rupture threshold is reached, the ICW content in the domain changes quickly causing the diffusivity to abruptly change and the downscaling model estimated the ICW content from the change in cell size. This resulted in a diffusivity range of $4\times10^{-10} – 2.58\times10^{-10}$ m^2/s which was slightly lower than the control model, Figure 7. The resulting diffusivities fell in the typically range of 10^{-11} and 10^{-9} m^2/s for food material (Panagiotou et al., 2004; Saravacos & Maroulis, 2001).

The macroscale domain shrunk from an initial size of 30mm in height and of 18mm in diameter to a height of 25.1mm and a diameter of 13mm when drying at 47°C and a height of 26.7mm and a diameter of 14.8mm when drying at 64°C. The macroscale shrinkage velocity was higher in the initial stages of drying and dramatically decreased in the later stage through considering the solid structure mobility factor, mimicking what occurs in the real world with the case hardening and the glass transition effect (Tuly et al., 2025). This results in varying shrinkage velocities of 2.24×10^{-7} to 2.9×10^{-8} for drying at 47°C and 2.96×10^{-7} to 1.23×10^{-8} for drying at 64°C. This nonlinear shrinkage can also be seen in Figure 9 and Figure 10. Drying at 47°C resulted in more deformation due to the longer drying time, aligning with previously published results (Gulati & Datta, 2015; Tuly et al., 2025).

[Figure 6 can be placed here]

[Figure 7 can be placed here]

3.4 Macroscale – Temperature evolution

The downscaling model accurately predicted the average sample temperature for drying at both 47°C and 64°C, with MREs of 0.66% and 0.90% respectively, Figure 8. Similarly, the control model achieved MREs of 0.46% and 0.89% respectively when compared to the experimental results, Figure 8. The downscaling model predicted the temperature evolution much more consistently when drying at 47°C than at 64°C. Although having a low MRE, the downscaling model predicted an unusual trend for drying 64°C, underpredicting and overpredicting the temperature throughout the drying time. The only notable difference between the downscaling model and the control model at both drying temperatures is the inclusion of moisture-dependent density in the downscaling model and macroscale deformation. Additionally, no properties within the heat transfer are in terms of ICW, rather

just macroscale moisture. Both the multiscale downscaling model and the control model significantly overpredicted the experimental data in the early stages of drying. It should be noted, the experimental data is of a sample under convective drying with perpendicular airflow on the x-y plane due to the location of the inlet and outlet within the dryer (shown in Figure B.1 in the supplementary material). Due to the perpendicular airflow, a large 'dead zone' existed behind the trailing edge of the sample during drying and thus, the heat transfer coefficient heavily effected in this region of the sample, demonstrate by Khan et al. (2020). Furthermore, in real life the heat and mass transfer coefficient also evolves as the sample shrinks corresponding to the change in its characteristic length (Welsh et al., 2021a). As a result, the temporally and spatially constant heat transfer coefficient contributed heavily to the initial overprediction.

[Figure 8 can be placed here]

3.5 Intracellular water transport

The spatial moisture profile at macroscale and the three locations of interest can be seen in Figure 9 and Figure 10 for drying at 47°C and 64°C respectively. Within this figure the dashed circle denotes the original cell size and the dashed rectangle denotes the original size of the macroscale domain. It should be noted, the moisture profile shown in Figure 9 and Figure 10 are at the exchange steps. As expected, each point of interest has its own temporal moisture profile corresponding to the macroscale conditions occurring at that particular point. This is unlike the existing microscale models in literature which utilize a single domain to characterize the sample transport (Rahman et al., 2018). As the moisture profile develops within the sample, the intracellular space at the outside point (P3), dries first. As expected, in the later stages, the intracellular space at P3 is almost entirely dry whereas the intracellular

space at P1 only starts to dry. This trend observed in both drying temperatures. Additionally, due to the temporal coupling and the size of the exchange time step utilized, there can be a delay in the moisture transfer between the end of the microscale and the initialization of the microscale. The microscale is only simulated for 5 seconds after an exchange step and the data exchange only occurs every 600 seconds (10 mins). This creates a time skip of 595 seconds. Evidence of this delay can be seen in the microscale at P3 at 100 minutes in Figure 9.

[Figure 9 can be placed here]

[Figure 10 can be placed here]

The average moisture content of the intracellular spaces at each point of interest can be found in Figure 11 (a). Throughout drying, the flux through the cell wall at P3 (point closest to the exterior wall) is significantly larger than the flux at P2 and P1, especially in the middle portion of drying. This trend is consistent for both drying temperatures. Furthermore, a comparison between the predicted ICW content and the predicted macroscale moisture content at each point interest can be seen in Figure 11 (b). The downscaling model preserves the average across the microscale domain at each point of interest, causing the ICW content to slightly lag behind the macroscale due to the intracellular space acting as an additional barrier or storage domain. The flux through the cell wall can be seen in Figure 12, where (a) shows the flux through the cell wall when the downscaling model does not consider macroscale deformation and (b) shows the downscaling model when macroscale deformation is considered. Both scenarios result in very different flux evolutions. When macroscale deformation is not considered the flux through the cell walls at each point exhibit peaks at different stages of drying and as expected drying at higher temperatures resulted in additional flux through the cell wall. P3 near the outside wall peaks first at 110 mins for drying at 64°C with a magnitude of -4.33×10^{-7} mol/m^{2}s. For drying at 47°C, P3's peak occurs later at 170

mins. Furthermore, the evolution of the macroscale and microscale moisture content distribution for simulating the downscaling model without deformation can in found in the Supplementary material (Appendix C). When macroscale deformation is considered, the cells and thus points of interest move as the domain shrinks. The points of interest move in proportion to the change in domain size (the points of interest are always assumed to be equally spaced along the sample). This assumption effects the resulting flux the cell wall experiences and result in the flux at each point of interest increasing over time, following a similar trend of the moisture content evolution, Figure 11 (a) and Figure 12 (b). Note the uneven flux in the later stages of drying at 64°C is related to the intracellular space moving in relation to the moisture gradient. When drying at 47°C, P1, P2 and P3 moved 0.62mm, 1.23mm and 1.84mm respectively towards the center of the domain. For drying at 64°C, P1, P2 and P3 moved 0.4mm, 0.81mm and 1.22mm respectively. The different shrinkage velocity for the two drying temperatures resulted in slightly different final cell sizes of 119 µm for drying at 47°C and 109 µm for 64°C following the trend uncovered in the X-ray µCT investigation. It should be noted, the shrinkage velocity approach results in ideal microscale shrinkage.

[Figure 11 can be placed here]

3.6 Sensitivity Investigation

A sensitivity analysis was conducted on a parameter with uncertainty, specifically on cell wall permeability, which was considered constant. Literature has demonstrate when drying at 70°C the average cell wall thickness of granny smith apples changes from 9.312µm when fresh to 4.685µm when dried (Joardder et al., 2015). This change mainly occurs when the FW content reduces surrounding an intracellular space and ICW begins to transport through the cell wall. Permeability is the diffusivity of a cell wall over its width, hence as diffusivity and the wall thickness changes uncertainty exists within permeability. To evaluate the sensitivity of the

downscaling model, the cell permeability was investigated by varying the utilized value by ±10% while drying at 47°C. This parameter was investigated in relation to the average macroscale moisture content (kg/kg dry basis), the intracellular water content (kg/kg dry basis) and the cell wall flux (mol/m^{2}s). Additionally, thermal conductivity has some uncertainty as multiple functions exist in literature and as a result a brief investigation can be found in Appendix D of the Supplementary material.

The downscaling model's sensitivity to cell wall permeability can be seen in Figure 13. The macroscale moisture content and the microscale ICW content were not sensitive to the change in cell wall permeability with their magnitudes and trend not changing. However, as permeability is key in the cellular boundary condition, the changes in permeability do influence the magnitude of the cell wall flux. Plus 10% results in an increase to the magnitude of the flux whereas minus 10% decrease the flux through the cell wall. The difference is significant and clearly evidenced for P3 but much smaller for P1and P2. Furthermore, the downscaling model was also sensitive to cell wall permeability when deformation was not considered (Supplementary material Appendix C).

[Figure 12 can be placed here]

4. Discussion

The downscaling model provides new insight into the transport of ICW while accurately predicting drying at 47°C and 64°C. When drying at lower temperatures (47°C) the consideration of a constant ICW with the upscaled diffusivity [Equation (16)] creates a fairly constant diffusivity which was sufficient to accurately predict drying. This finding is consistent with pre-existing literature (Defraeye & Verboven, 2017; Welsh et al., 2023). When drying at medium temperatures (64°C), the multiscale downscaling model accurately predicted drying,

suggesting that ICW estimation based on cell size changes is suitable to utilize the upscaled diffusivity property with the rupture threshold. This technique enhances the generalizability of the modeling approach and differs from previously published work (Welsh et al., 2023). Notably, the shrinkage velocity approach, based on X-ray μCT data, was employed to estimate cell size changes. The model could be further refined by incorporating a physics-based approach to cellular deformation, such as van der Sman et al. (2024)'s recent work on pore development in viscoelastic foods during drying.

The microscales at the three points of interest provided interesting insight, Figure 9 to Figure 10. Each produced spatially dependent microscales which is different to the previously published microscale models where a single microscale is used to predict the material's evolution (Rahman et al., 2018). The flux evolution was very unique for each intracellular space at each point of interest. The microscale near the outside edge (P3) experienced significantly more flux throughout the entire duration of drying. The magnitude of the flux also depended on the drying air temperature and is sensitive to the magnitude of the cell wall permeability. Additionally, the flux through the cell wall (shown in Figure 12) was very dependent on how the points of interest (intracellular spaces) are considered in relation to the macroscale deformation, i.e. do the intracellular spaces remain at the same location within the macroscale domain when shrinkage occurs, do the intracellular spaces shrink and move as the macroscale domain shrinks and the material's porosity increases, and/or if the intracellular spaces do move, at what rate? This is evidence when comparing the flux evolution of the downscaling model with and without deformation [Figure 12 (a) and Figure 12(b)]. This work assumed the points of interest and thus intracellular spaces were always equally distributed along the domain. This assumption results in the intracellular spaces moving towards the center of the macroscale domain in relation to the shrinkage occurring, mimicking what occurs in relation to shrinkage and the materials porosity evolution. If a different assumption is

considered, it would likely result in a different evolution of flux. Literature has demonstrated when drying at medium temperature (above 50°C), progressive and ultimate cell rupturing would have occurred (Khan et al., 2018). It is theorized, due to the convective heating profile, when the surface reaches 50°C the intracellular space near the surface lose their rigidity and tend to become droopy, hence nearing their rupturing limit (Khan et al., 2018). The intracellular spaces lose turgor pressure and tend to fail due to the imposed thermal stress of continuous penetration of heat energy. Though past research on cell rupturing has been conducted using nuclear magnetic resonance which is only able to produce results of the entire sample (domain averages) and does not give insight into the spatial propagation of the rupturing mechanism. Further investigation is needed in the future, but the cell wall flux may provide valuable insight in predicting when and/or where cell rupturing spatially propagates within PBFMs.

One key component of any multiscale model is its temporal coupling. Previous works within the field (Rahman et al., 2018) have only utilized multiscale modeling to upscale properties. Such an approach produces a property, often a homogenized property, through computing the microscale in a steady state condition for specific discrete points of interest (i.e. when a cell has a moisture content of 3 kg/kg dry basis). However, as the current study is a multiscale downscaling model, the microscale evolves with time and hence a temporal coupling is required. Specifically, the HMM approach was utilized. This approach saves on computational cost but does not simulate the microscale for the entire simulation (as described in 2.3.1 Macro-micro temporal coupling). Instead, the approach just computes the microscale for a small period of time after the exchange point. Hence, there is a portion of time (9.16 mins) which is skipped in between the exchange steps. This saves on computational cost however it can create a delayed effect on the transport, which will not always be desired. Depending on the purpose of the model and the available computational resources, this skipped time can be either reduced or increased. Alternatively, temporal couplings like the continuous HMM

simulate the microscale across the entire time period and can be employed based on the model's purpose.

5. Conclusion

The multiscale model accurately described the drying process at both low and medium temperatures (47°C and 64°C). Furthermore, the integration of downscaling coupling in the model provided valuable insights into the microscale evolution during drying. When drying at medium temperatures, the rupturing threshold was reached and the ICW of the sample was predicted considering the changes in the cells size. To demonstrate the capacity of the approach, microscales at three points of interest were investigated. Each microscale evolved differently depending on the applied drying conditions and their spatial location within the domain. The ICW trend through the cell wall provided important insight into what the cell wall experiences at different locations and was also unique for each microscale location and drying temperature. Additionally, the convective drying temperature significantly influenced the magnitude of the flux the cell wall experienced due to the moisture migration. Further investigating is required but such a multiscale approach could be utilized to investigate how cell rupturing propagates within a domain. The model could also be refined to calculate cellular deformation through a more mathematical approach with deformation on both spatial scales coupled with some consideration of cell rupturing. Additionally, the microscale could be extended to 3D. The multiscale downscaling approach, coupled with Welsh et al. (2023) upscaling technique will facilitate the construct of an in-depth concurrent multiscale model being developed in the future.

Acknowledgements

This research work is supported by Australian Research council (DP220103668). The authors would like to acknowledge Dr. M.U.H Joardder for his suggestion in relation to the

cellular transport. Moreover, the authors also wish to express their gratitude to the KG-Q Research Facility, QUT for allowing access to the X-ray μCT equipment.

6. References

Asabe, J., & Home, A. American society of agricultural and biological engineers.

Auriault, J.-L., Boutin, C., & Geindreau, C. (2010). *Homogenization of coupled phenomena in heterogenous media* (Vol. 149). John Wiley & Sons.

Białobrzewski, I. (2006, 2006/08/01/). Simulation of changes in the density of an apple slab during drying. *International Communications in Heat and Mass Transfer, 33*(7), 880-888. https://doi.org/10.1016/j.icheatmasstransfer.2006.02.017

Carr, E. J., & Turner, I. W. (2014). Two-scale computational modelling of water flow in unsaturated soils containing irregular-shaped inclusions. *International Journal for Numerical Methods in Engineering*, *98*, 157-173. https://doi.org/10.1002/nme.4625

Carr, E. J., Turner, I. W., & Perré, P. (2013). A dual-scale modeling approach for drying hygroscopic porous media. *Multiscale Modeling & Simulation, 11*, 362-384. https://doi.org/10.1137/120873005

Cengel, Y. (2003). *Heat, Transfer Mass: A practical approach*. Mc-Graw Hill Education, Columbus, GA, USA.

Cengel, Y. A., & Boles, M. A. (2002). Thermodynamics: an engineering approach. *Sea, 1000*, 8862.

Defraeye, T., & Radu, A. (2018). Insights in convective drying of fruit by coupled modeling of fruit drying, deformation, quality evolution and convective exchange with the airflow. *Applied Thermal Engineering, 129*, 1026-1038. https://doi.org/10.1016/j.applthermaleng.2017.10.082

Defraeye, T., & Verboven, P. (2017, 2017/01/01/). Convective drying of fruit: Role and impact of moisture transport properties in modelling. *Journal of Food Engineering, 193*, 95-107. http://dx.doi.org/10.1016/j.jfoodeng.2016.08.013

662 Fanta, S. W., Abera, M. K., Aregawi, W. A., Ho, Q. T., Verboven, P., Carmeliet, J., & Nicolai,
663 B. M. (2014). Microscale modeling of coupled water transport and mechanical
664 deformation of fruit tissue during dehydration. *Journal of Food Engineering*, *124*, 86-
665 96. https://doi.org/10.1016/j.jfoodeng.2013.10.007

666 Fanta, S. W., Abera, M. K., Ho, Q. T., Verboven, P., Carmeliet, J., & Nicolai, B. M. (2013).
667 Microscale modeling of water transport in fruit tissue. *Journal of Food Engineering*,
668 *118*, 229-237. https://doi.org/10.1016/j.jfoodeng.2013.04.003

669 Ferrando, M., & Spiess, W. E. L. (2001, 2001/08/01/). Cellular response of plant tissue during
670 the osmotic treatment with sucrose, maltose, and trehalose solutions. *Journal of Food*
671 *Engineering*, *49*(2), 115-127. https://doi.org/10.1016/S0260-8774(00)00218-1

672 Golestani, R., Raisi, A., & Aroujalian, A. (2013). Mathematical modeling on air drying of
673 apples considering shrinkage and variable diffusion coefficient. *Drying Technology*,
674 *31*, 40-51. https://doi.org/10.1080/07373937.2012.714826

675 Gulati, T., & Datta, A. K. (2015, 2015/12/01/). Mechanistic understanding of case-hardening
676 and texture development during drying of food materials. *Journal of Food Engineering*,
677 *166*, 119-138. https://doi.org/10.1016/j.jfoodeng.2015.05.031

678 Halder, A., Datta, A. K., & Spanswick, R. M. (2011). Water transport in cellular tissues during
679 thermal processing. *AIChE Journal*, *57*(9), 2574-2588.
680 https://doi.org/10.1002/aic.12465

681 Joardder, M. U., Brown, R. J., Kumar, C., & Karim, M. (2015). Effect of cell wall properties
682 on porosity and shrinkage of dried apple. *International Journal of Food Properties*,
683 *18*(10), 2327-2337. https://doi.org/10.1080/10942912.2014.980945

684 Joardder, M. U. H., & Karim, M. A. (2019, 2019/11/18). Development of a porosity prediction
685 model based on shrinkage velocity and glass transition temperature. *Drying*
686 *Technology*, *37*(15), 1988-2004. https://doi.org/10.1080/07373937.2018.1555540

687 Karunasena, H. C. P., Gu, Y. T., Brown, R. J., & Senadeera, W. (2015, 2015/04/01/).
688 Numerical investigation of plant tissue porosity and its influence on cellular level
689 shrinkage during drying. *Biosystems Engineering*, *132*(Supplement C), 71-87.
690 https://doi.org/10.1016/j.biosystemseng.2015.02.002

691 Khan, M. I. H., Farrell, T., Nagy, S. A., & Karim, M. A. (2018, 2018/10/12). Fundamental
692 Understanding of Cellular Water Transport Process in Bio-Food Material during
693 Drying. *Scientific Reports, 8*(1), 15191. https://doi.org/10.1038/s41598-018-33159-7

694 Khan, M. I. H., Wellard, R. M., Nagy, S. A., Joardder, M. U. H., & Karim, M. A. (2016,
695 2016/12/01/). Investigation of bound and free water in plant-based food material using
696 NMR T2 relaxometry. *Innovative Food Science & Emerging Technologies, 38*, 252-
697 261. https://doi.org/10.1016/j.ifset.2016.10.015

698 Khan, M. Imran H., Welsh, Z., Gu, Y., Karim, M. A., & Bhandari, B. (2020, 2020/06/01/).
699 Modelling of simultaneous heat and mass transfer considering the spatial distribution
700 of air velocity during intermittent microwave convective drying. *International Journal*
701 *of Heat and Mass Transfer, 153*, 119668.
702 https://doi.org/10.1016/j.ijheatmasstransfer.2020.119668

703 Mattea, M., Urbicain, M. J., & Rotstein, E. (1986, 1986/01/01). Prediction of Thermal
704 Conductivity of Vegetable Foods by the Effective Medium Theory. *Journal of Food*
705 *Science, 51*(1), 113-115. https://doi.org/10.1111/j.1365-2621.1986.tb10848.x

706 Mbarek, R., & Mihoubi, D. (2019). Development of physical properties of apple during
707 dehydration. *Periodica Polytechnica Chemical Engineering, 63*(4), 591-599.

708 Moshelion, M., Moran, N., & Chaumont, F. (2004, Aug). Dynamic changes in the osmotic
709 water permeability of protoplast plasma membrane. *Plant Physiol, 135*(4), 2301-2317.
710 https://doi.org/10.1104/pp.104.043000

711 Pace, E. L. (1962, 1962/08/01). Scientific foundations of vacuum technique (Dushman, Saul).
712 *Journal of Chemical Education, 39*(8), A606. https://doi.org/10.1021/ed039pA606

713 Panagiotou, N., Krokida, M., Maroulis, Z., & Saravacos, G. (2004). Moisture diffusivity:
714 literature data compilation for foodstuffs. *International Journal of Food Properties,*
715 *7*(2), 273-299. https://doi.org/10.1081/JFP-120030038

716 Pavliotis, G. A., & Stuart, A. (2008). *Multiscale methods: averaging and homogenization*.
717 Springer Science & Business Media.

718 Perré, P. (2007). Multiscale aspects of heat and mass transfer during drying. *Transport in*
719 *Porous Media, 66*, 59-76. https://doi.org/10.1007/s11242-006-9022-2

720 Perré, P. (2019, 2019/09/01/). Coupled heat and mass transfer in biosourced porous media
721 without local equilibrium: A macroscopic formulation tailored to computational
722 simulation. *International Journal of Heat and Mass Transfer, 140*, 717-730.
723 https://doi.org/10.1016/j.ijheatmasstransfer.2019.06.043

724 Prawiranto, K., Carmeliet, J., & Defraeye, T. (2020). Identifying in silico how microstructural
725 changes in cellular fruit affect the drying kinetics [10.1039/D0SM00749H]. *Soft*
726 *Matter, 16*(43), 9929-9945. https://doi.org/10.1002/nme.462510.1039/D0SM00749H

727 Prawiranto, K., Defraeye, T., Derome, D., Verboven, P., Nicolai, B., & Carmeliet, J. (2018,
728 2018/12/01/). New insights into the apple fruit dehydration process at the cellular scale
729 by 3D continuum modeling. *Journal of Food Engineering, 239*, 52-63.
730 https://doi.org/10.1016/j.jfoodeng.2018.06.023

731 Qiu, S., Xu, S., Rao, B., Mujumdar, A. S., & Xu, P. (2022, 2022/12/01/). A multi-scale model
732 for impingement drying of porous slab. *Journal of Food Engineering, 335*, 111194.
733 https://doi.org/10.1016/j.jfoodeng.2022.111194

734 Rahman, M. M., Kumar, C., Joardder, M. U. H., & Karim, M. A. (2018, 9/21/). A micro-level
735 transport model for plant-based food materials during drying. *Chemical Engineering*
736 *Science, 187*, 1-15. https://doi.org/10.1016/j.ces.2018.04.060

737 Ratti, C., Crapiste, G., & Rotstein, E. (1989). A new water sorption equilibrium expression for
738 solid foods based on thermodynamic considerations. *Journal of Food Science, 54*(3),
739 738-742. https://doi.org/10.1111/j.1365-2621.1989.tb04693.x

740 Saravacos, G. D., & Maroulis, Z. B. (2001). *Transport properties of foods*. CRC Press.

741 Tan, L., Yuan, Y., Zhao, Z., Xu, Y., & Yuan, Y. (2023, 2023/06/01/). Insights in mechanism
742 of drying shrinkage by pore-scale modeling of heat-moisture and stress-strain
743 distribution for high-moisture porous media. *International Journal of Thermal*
744 *Sciences, 188*, 108226. https://doi.org/10.1016/j.ijthermalsci.2023.108226

745 Tuly, S. S., Joardder, M. U. H., Welsh, Z. G., & Karim, A. (2023). Mathematical Modelling of
746 Heat and Mass Transfer during Jackfruit Drying Considering Shrinkage. *Energies,*
747 *16*(11), 4461. https://www.mdpi.com/1996-1073/16/11/4461

748 Tuly, S. S., Joardder, M. U. H., Welsh, Z. G., & Karim, A. (2025, 2025/02/01/). A novel
749 mechanistic model for predicting shrinkage kinetics in plant-based foods by integrating

solid matrix mobility and viscoelasticity. *Journal of Food Engineering*, *387*, 112346. https://doi.org/10.1016/j.jfoodeng.2024.112346

van der Sman, R., Curatolo, M., & Teresi, L. (2024). Pore development in viscoelastic foods during drying [10.1039/D4SM00201F]. *Soft Matter*, *20*(26), 5183-5194. 10.1039/D4SM00201F

Vega-Mercado, H., Marcela Góngora-Nieto, M., & Barbosa-Cánovas, G. V. (2001, 2001/09/01/). Advances in dehydration of foods. *Journal of Food Engineering*, *49*(4), 271-289. https://doi.org/10.1016/S0260-8774(00)00224-7

Weligama Thuppahige, V. T., Welsh, Z. G., Joardder, M., & Karim, A. (2024, 2024/01/01/). Recent advances in determining the cellular-level property evolutions of plant-based food materials during drying. *Trends in Food Science & Technology*, *143*, 104291. https://doi.org/10.1016/j.tifs.2023.104291

Welsh, Z., Simpson, M. J., Khan, M. I. H., & Karim, M. (2018). Multiscale Modeling for Food Drying: State of the Art. *Comprehensive Reviews in Food Science and Food Safety*, *17*(5), 1293-1308. https://doi.org/10.1111/1541-4337.12380

Welsh, Z. G., Khan, M. I. H., & Karim, M. (2021a). Multiscale modeling for food drying: A homogenized diffusion approach. *Journal of Food Engineering*, *292*, 110252. https://doi.org/10.1016/j.jfoodeng.2020.110252

Welsh, Z. G., Simpson, M. J., Khan, M. I. H., & Karim, A. (2021b). A multiscale approach to estimate the cellular diffusivity during food drying. *Biosystems Engineering*, *212*, 273-289. https://doi.org/10.1016/j.biosystemseng.2021.10.017

Welsh, Z. G., Simpson, M. J., Khan, M. I. H., & Karim, M. A. (2023, 2023/03/01/). Generalized moisture diffusivity for food drying through multiscale modeling. *Journal of Food Engineering*, *340*, 111309. https://doi.org/10.1016/j.jfoodeng.2022.111309

Whitaker, S. (1977). Simultaneous Heat, Mass, and Momentum Transfer in Porous Media: A Theory of Drying. *Advances in Heat Transfer*, *13*, 119-203. http://dx.doi.org/10.1016/S0065-2717(08)70223-5

779 **Figures:**

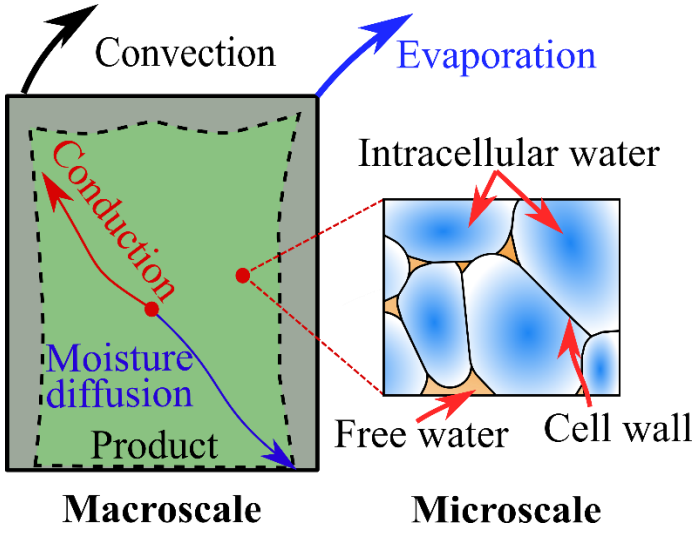

780

781 Figure 1. Cellular structure of plant-based food material

782

783

784

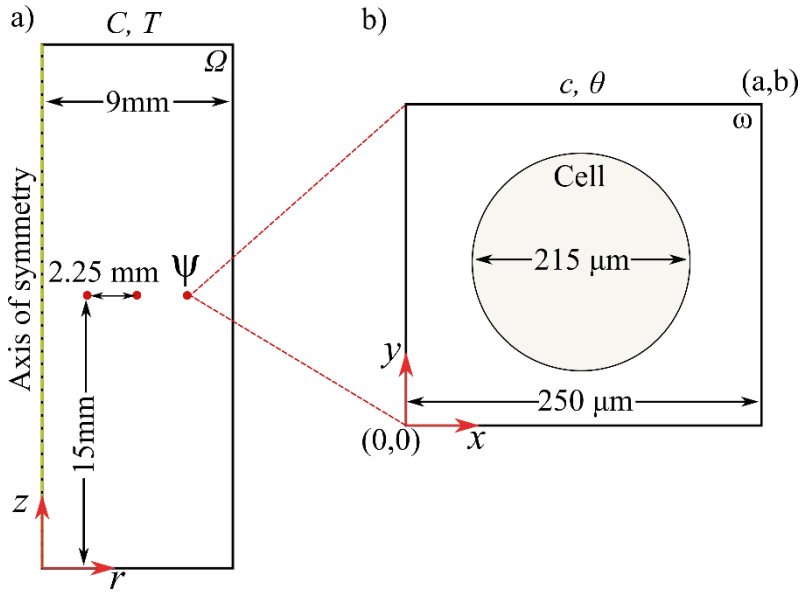

785

786 Figure 2. Domains, a) axisymmetric macroscale domain with the three locations of

787 interest marked by red dots, and b) microscale domain.

788

789

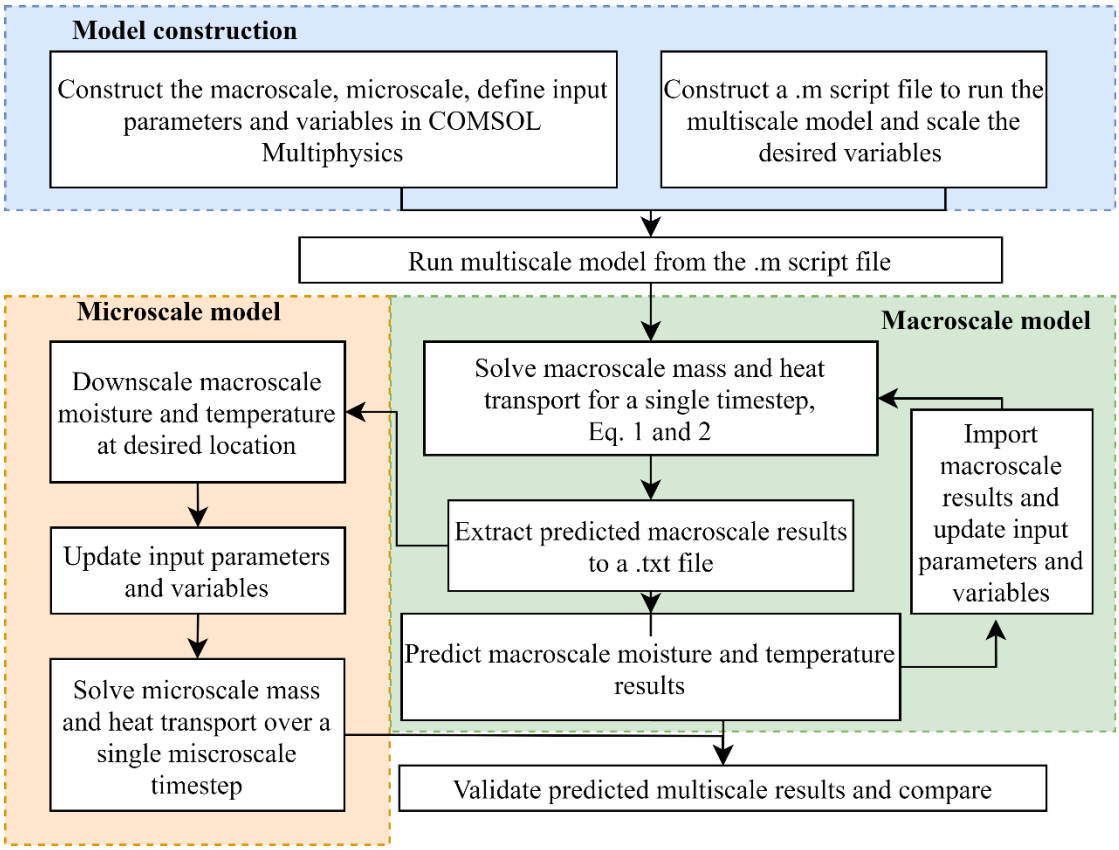

790

791 Figure 3. Simulation Methodology

792

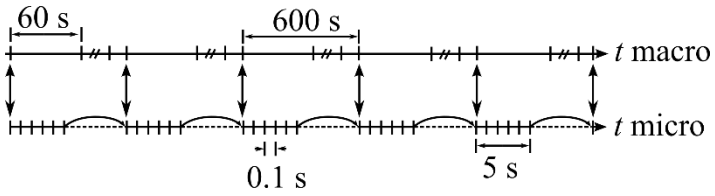

Figure 4. Multiscale temporal coupling.

798

799

a) b) c)

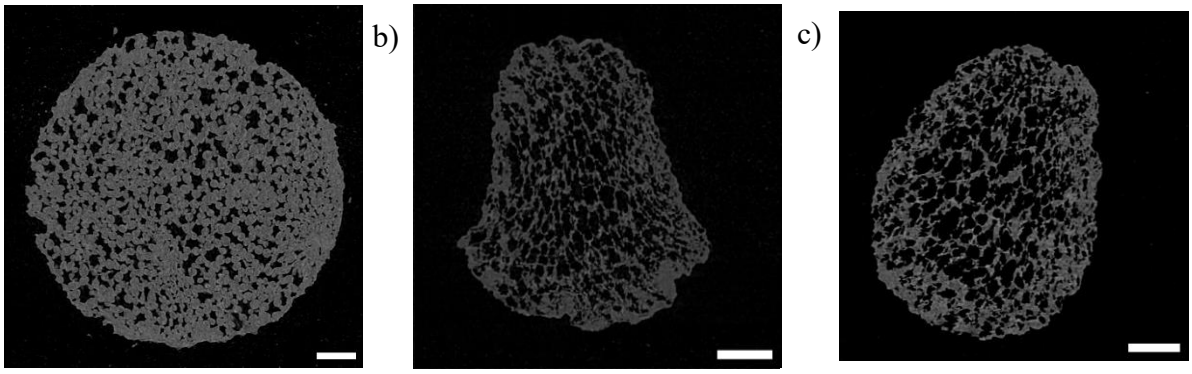

800

801 Figure 5. X-ray µCT images of, (a) fresh, (b) dried at 45°C at 0.8 kg/kg dry basis, (b)
802 dried at 60°C at 1.23 kg/kg dry basis. The white scalebar represents 1mm in each
803 corresponding image.

804

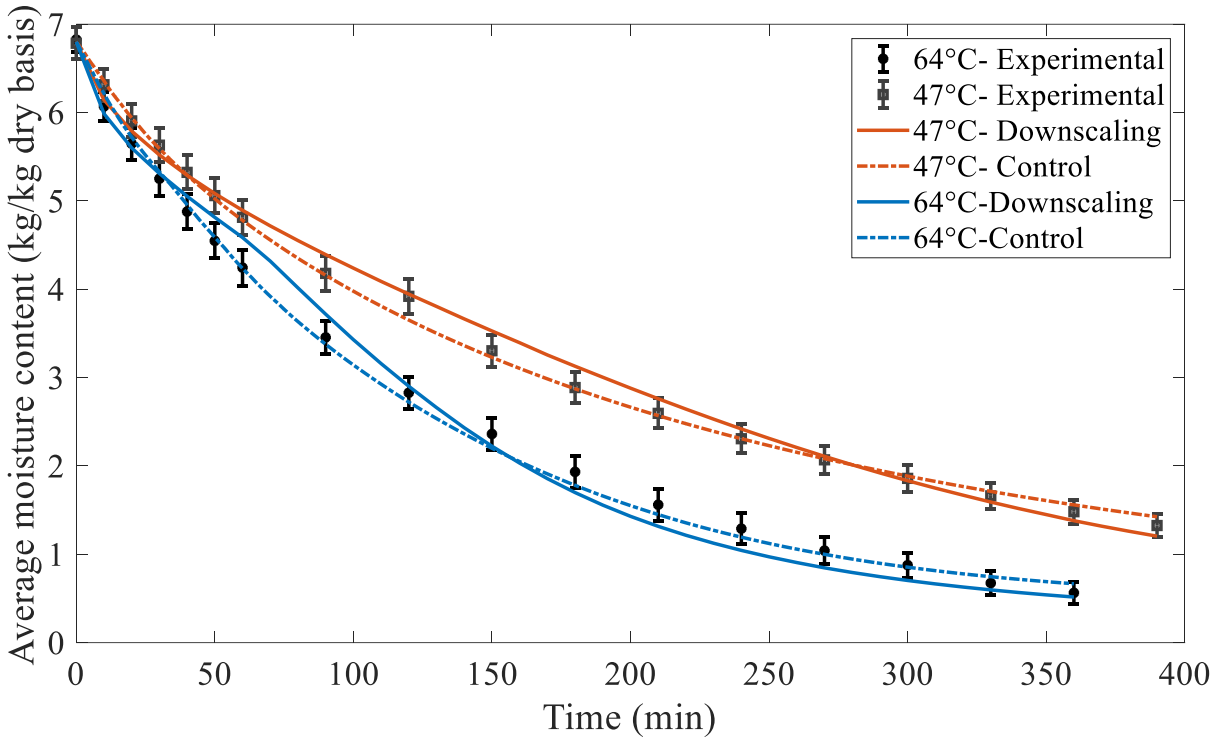

805

806 Figure 6. Average macroscale moisture content (kg/kg dry basis) at low and medium

807 temperature drying.

808

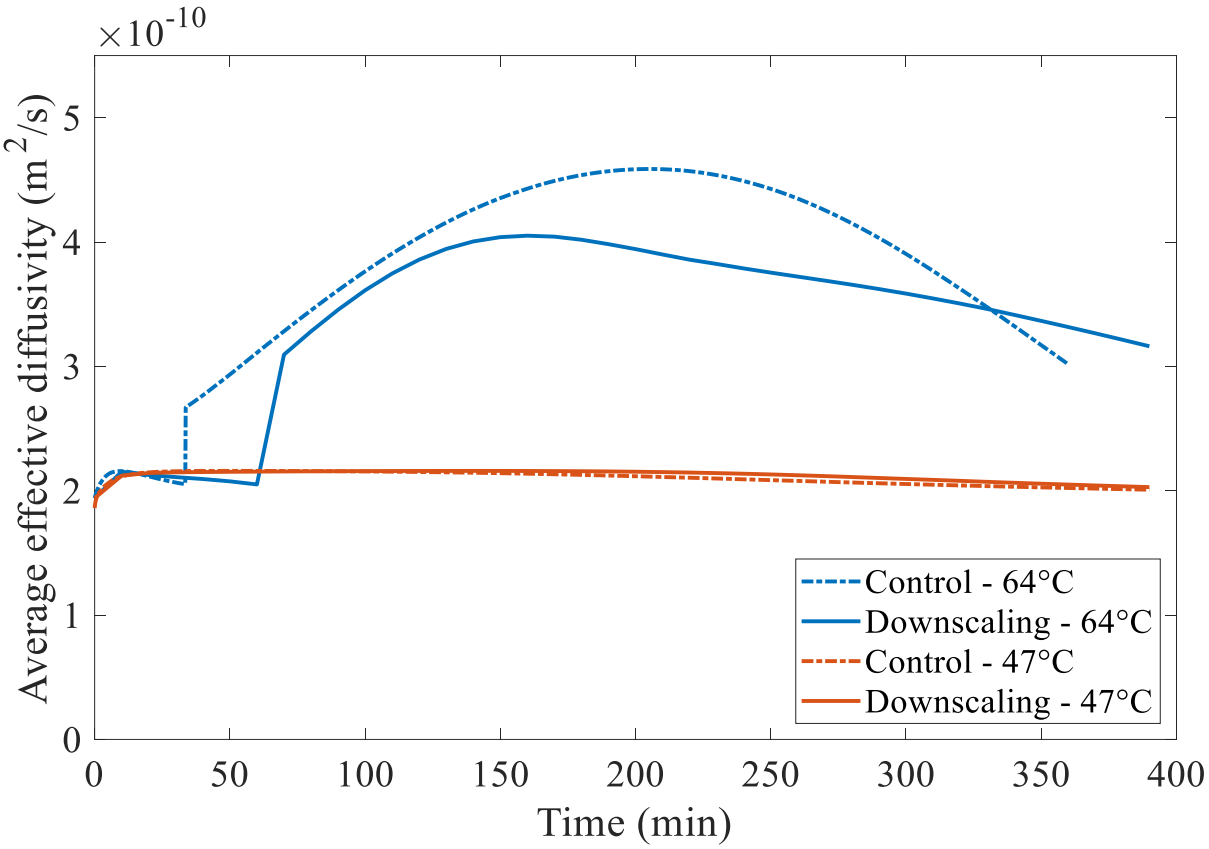

809

810 Figure 7. Average macroscale diffusivity (m^2/s), Equation (16), for both drying temperatures.

811

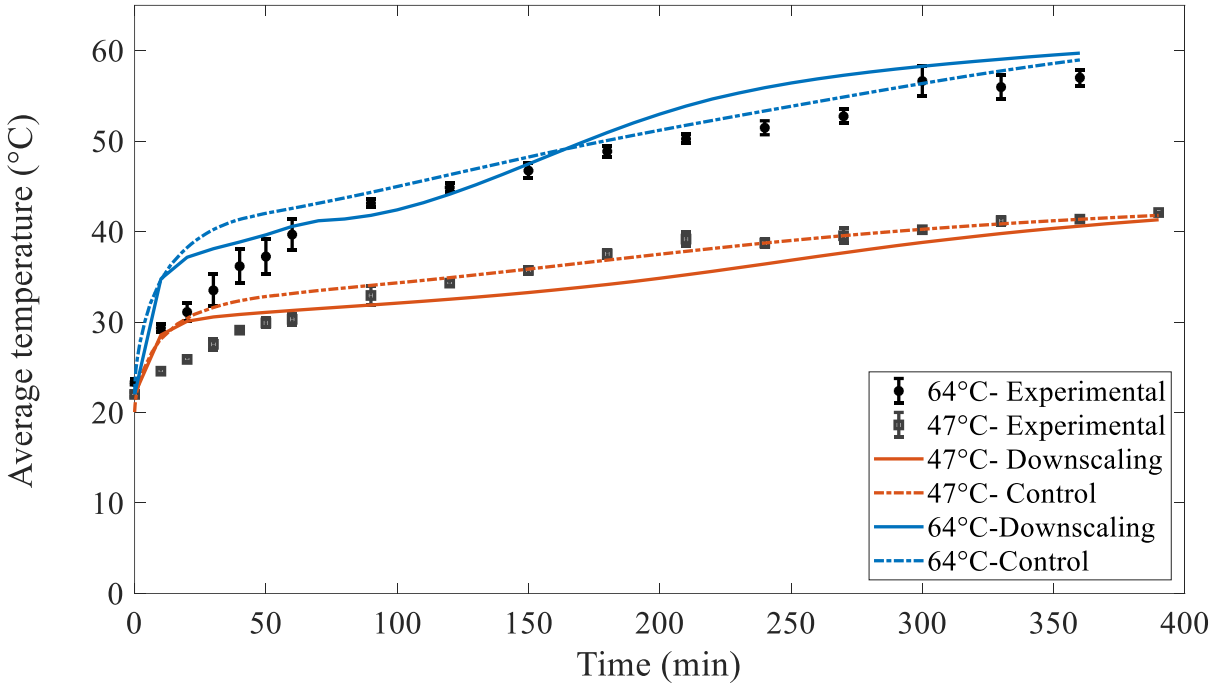

812

813 Figure 8. Average macroscale surface temperature (°C) for both drying temperatures.

814

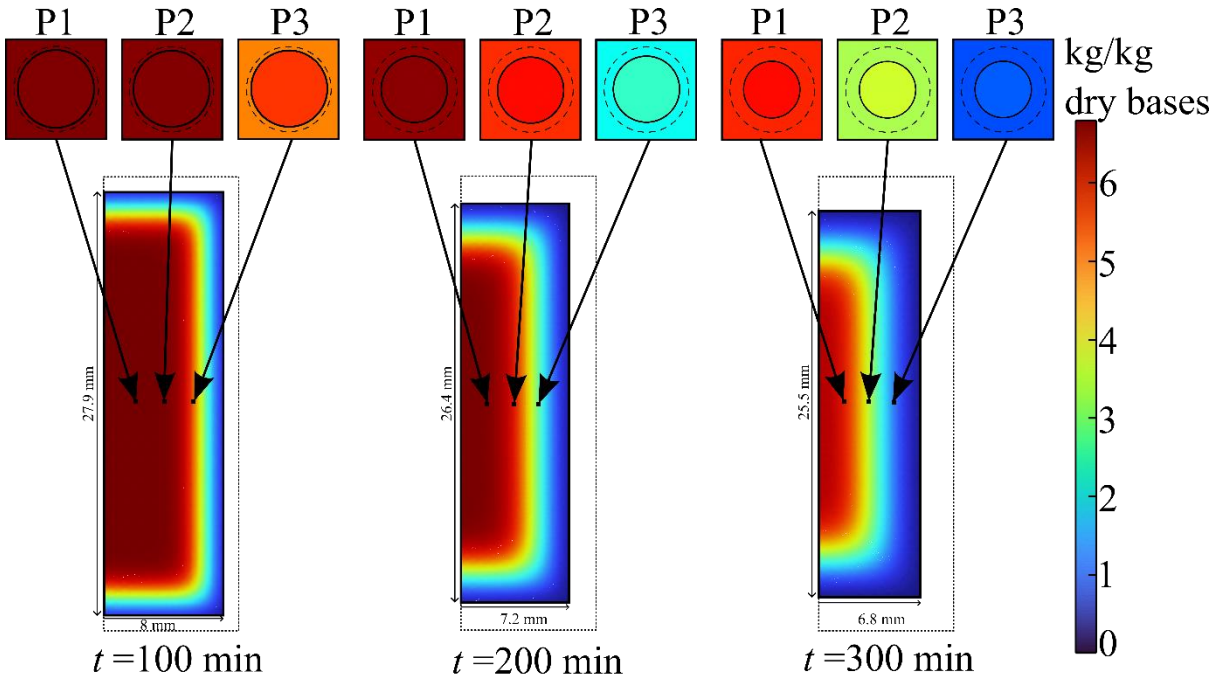

815

816 Figure 9. Multiscale moisture distribution (kg/kg dry basis) for drying at 47°C. Original cell

817 and macroscale geometries visually represented by the dashed circle and dashed rectangle.

818

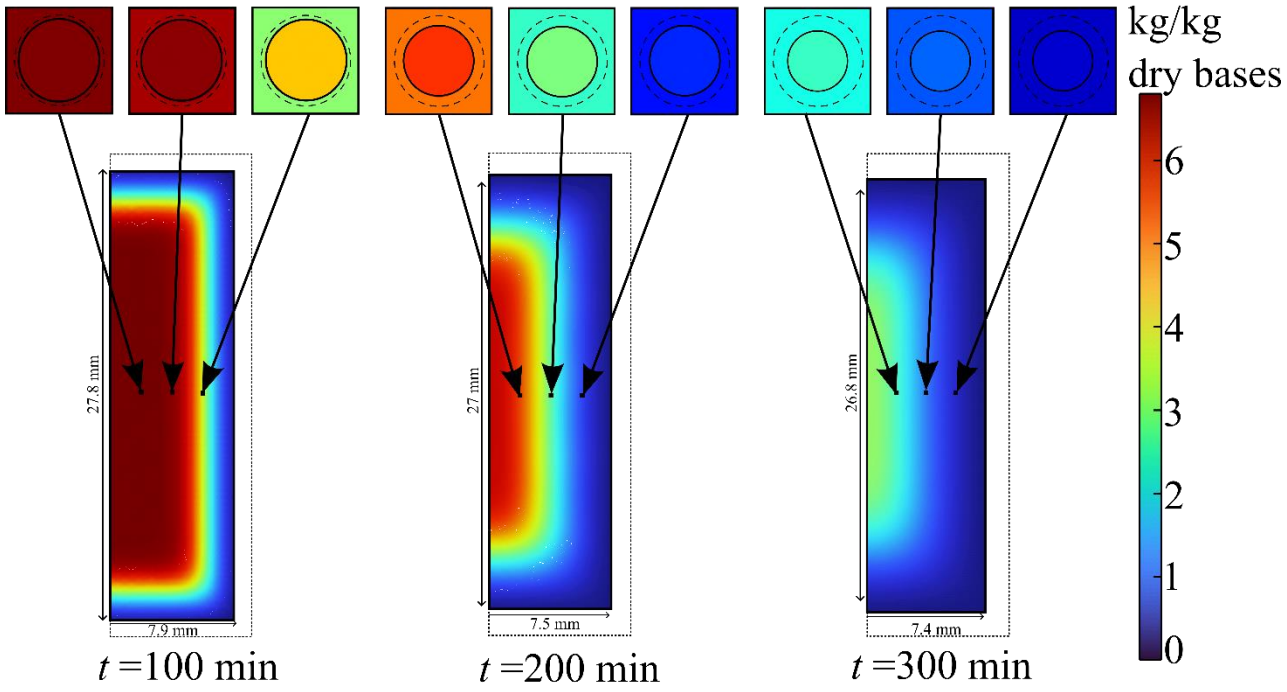

819

820 Figure 10. Multiscale moisture distribution (kg/kg dry basis) for drying at 64°C. Original cell

821 and macroscale geometries visually represented by the dashed circle and dashed rectangle.

822

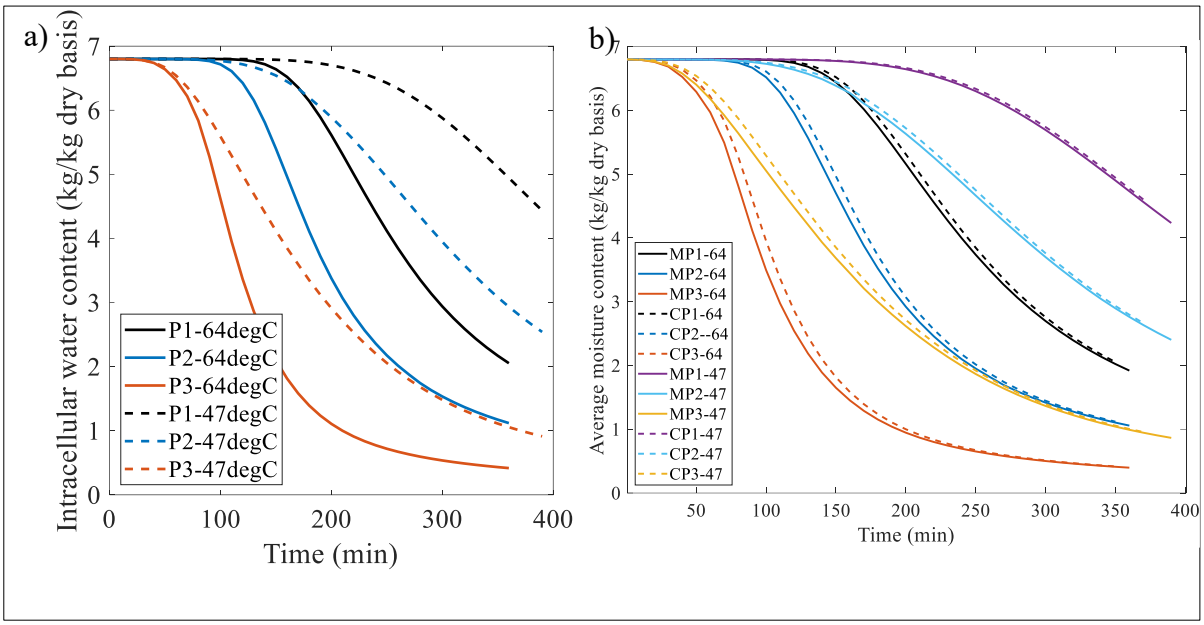

823

824 Figure 11. Intracellular water evolution for both drying temperatures, (a) concentration within
825 each intracellular space at the points of interest (kg/kg dry basis), (b) comparing the
826 intracellular water content and the macroscale water content (kg/kg dry basis) at each point of
827 interest where M denotes the macroscale and C denote the intracellular water content.

828

829

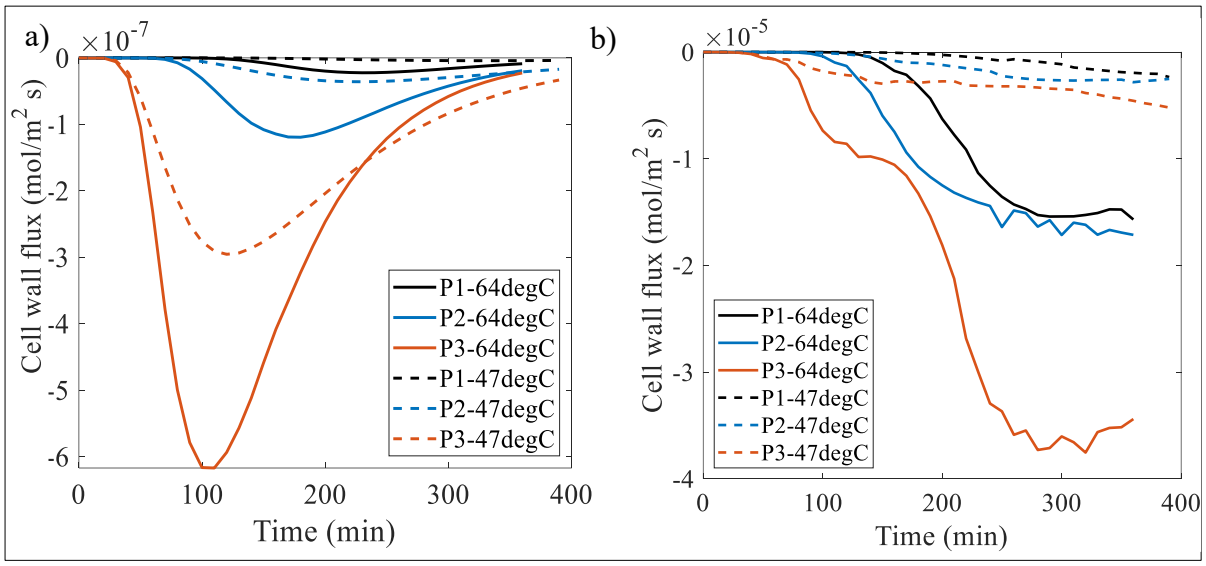

830

831 Figure 12. Flux evolution of the intracellular water through the cell wall (mol m^{-2} s^{-1}) at the

832 points of interest for both drying temperatures, (a) without macroscale deformation (b) with

833 macroscale deformation.

834

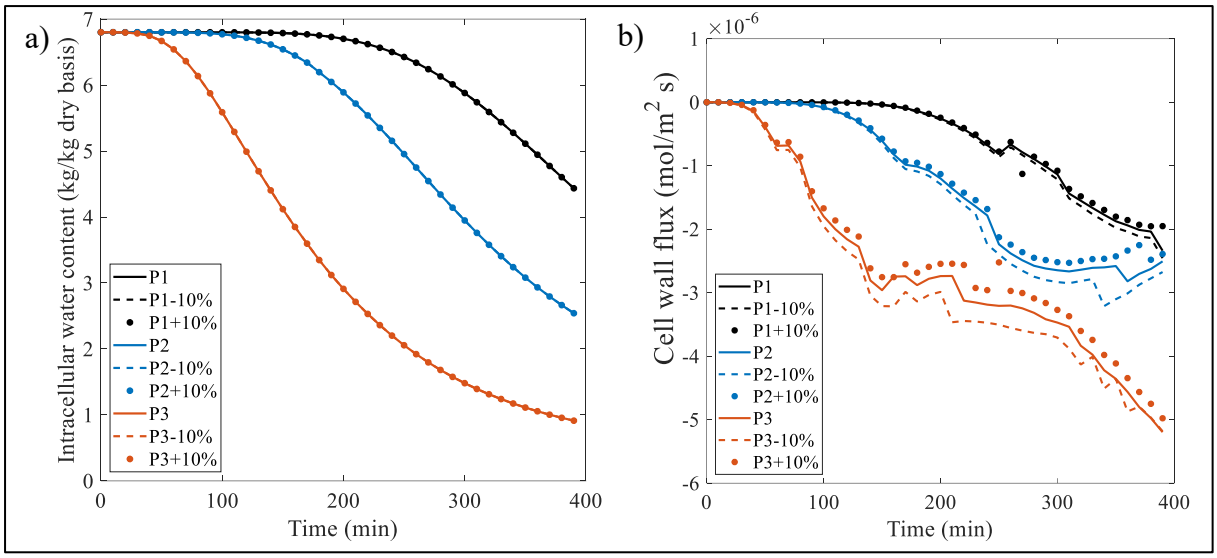

Figure 13. Sensitivity investigation for the cell wall permeability ±10%, a) moisture content (kg/kg dry basis), at each point of interest b) cell wall flux (mol/m^{2}s) at each point of interest.

839 **Tables:**

840 Table 1. Input parameters

Parameter	Value (unit)	Reference
Density of apple, ρ	$-7.301M_{db}^2+92.552M_{db}+450.53$	(Mbarek & Mihoubi, 2019)
Density of water, ρ_w	995 (kg m^{-3})	Cengel (2003)
Specific heat of apple, c_p	$1000(1.4+3.22M_{wb})$ (J kg^{-1} K^{-1})	Białobrzewski (2006)
Thermal conductivity of apple, k	$0.49-0.443\exp(-0.206M_{db})$ (W/(m·K))	Mattea et al. (1986)
Initial moisture content, M_0	6.8 (kg kg^{-1} dry basis)	This study
Initial sample temperature, T_0	296 (K)	This study
Glass transition temperature of water, T_{gw}	138.15 (K)	(Joardder & Karim, 2019)
Initial glass transition temperature, T_{g0}	165 (K)	(Joardder & Karim, 2019)
Gordon and Taylor constant, k_c	3.4	(Joardder & Karim, 2019)
Initial wet basis moisture content, $M_{o_{wb}}$	0.86 (kg kg^{-1} wet basis)	This study
Latent heat of evaporation, h_{fg}	2358600 (J kg^{-1})	Cengel (2003)
Universal gas constant, R	8.314 (J mol^{-1} K^{-1})	Cengel and Boles (2002)

Molar mass of water, M_w	0.018016 (kg mol^{-1})	Cengel and Boles (2002)
Partial vapor pressure, $p_{v\ air}$	1250 (Pa)	(Welsh et al., 2023)
Heat transfer coefficient, h_T	18 (W m^{-2} K^{-1})	This study
Cell wall permeability	2 x 10^{-5} (m s^{-1})	(Ferrando & Spiess, 2001; Moshelion et al., 2004)

841

Supplementary Material

Appendix A - Converting concentrations to wet and dry bases.

The wet and dry moisture contents were considered as,

$$M_{wb} = \frac{C M_w}{\rho} \tag{A.1}$$

$$M_{db} = \frac{M_{wb}}{1 - M_{wb}} \tag{A.2}$$

where M_{wb} is the wet bases moisture content (kg/kg wet basis), M_{db} is the dry bases moisture content (kg/kg dry basis), C is the instantaneous moisture concentration (mol/m^3), ρ is the density of the material (kg/m^3) and M_w molar mass of water (kg/mol).

Appendix B – Experimental drying set up

The experimental drying set up used within this work can be seen in Figure B.1. Within this experimental set up the sample experiences perpendicular airflow along the x-y plane due to the location of the inlet and outlet locations in relation to the sample (inlet is on the samples left and outlet is at its back). It should be noted, the experimental dryer also has microwave capabilities which was not active during the convective drying experiments.

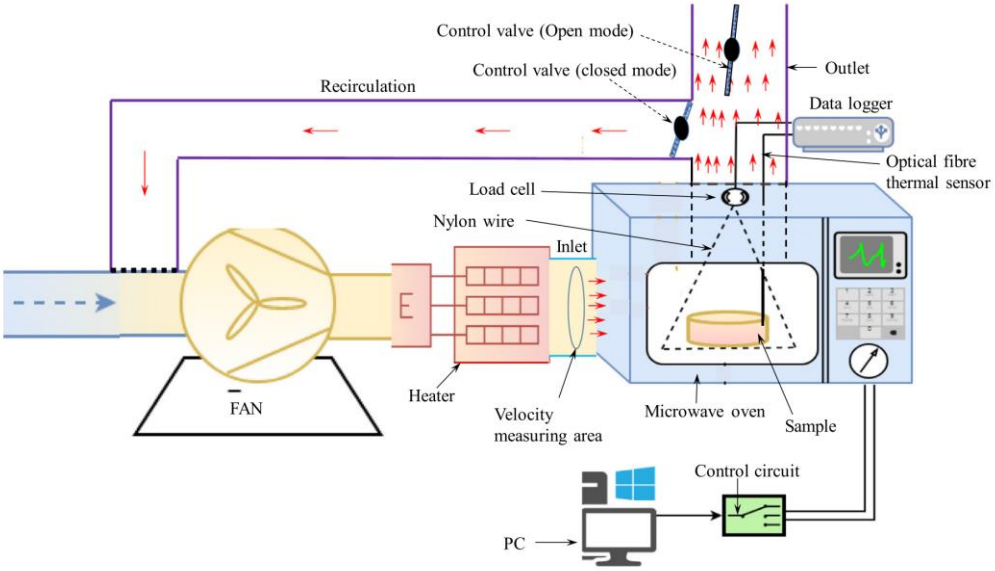

Figure B.1 Schematic diagram of the experimental drying setup used

Appendix C – Moisture distribution of the downscaling model without deformation

The moisture distribution at both scales of the downscaling model without macroscale deformation can be seen in Figure C.1 and Figure C.2.

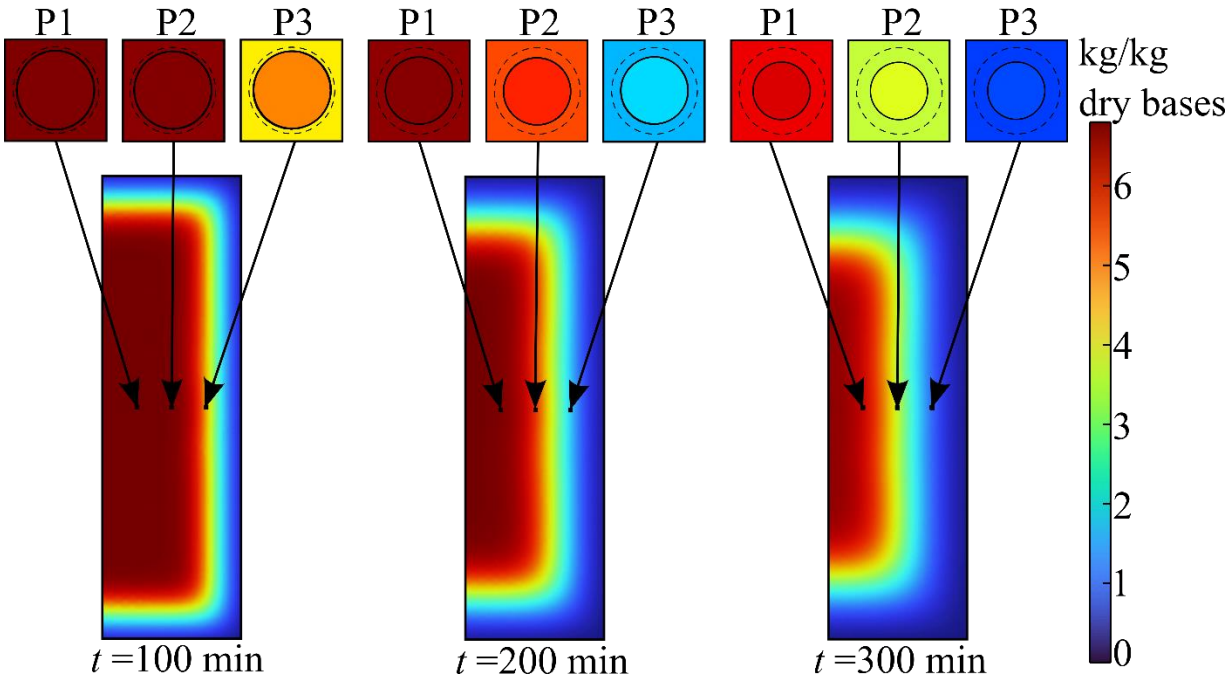

Figure C.1. Multiscale moisture distribution (kg/kg dry bases) for drying at 47°C. Original cell geometry visually represented by the dashed circle.

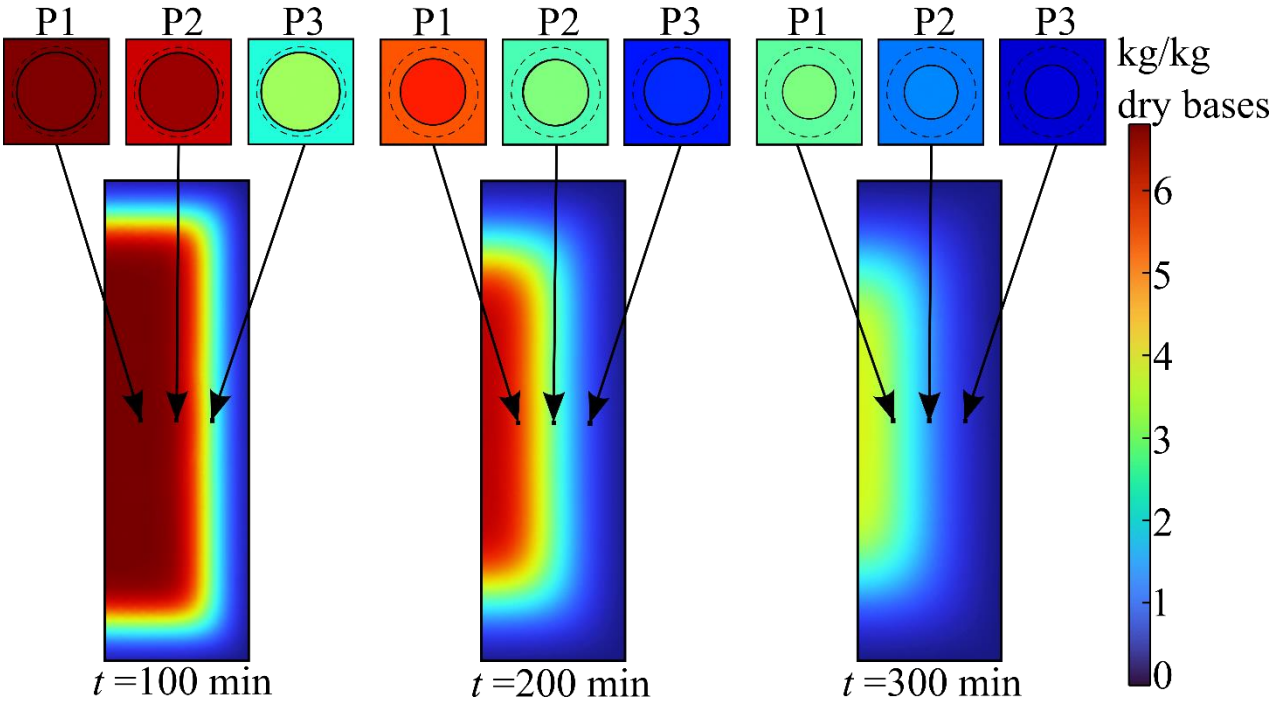

Figure C.3. Multiscale moisture distribution (kg/kg dry bases) for drying at 64°C. Original cell geometry visually represented by the dashed circle.

The sensitivity investigation for the downscaling model without considering deformation can be seen in Figure C.3.

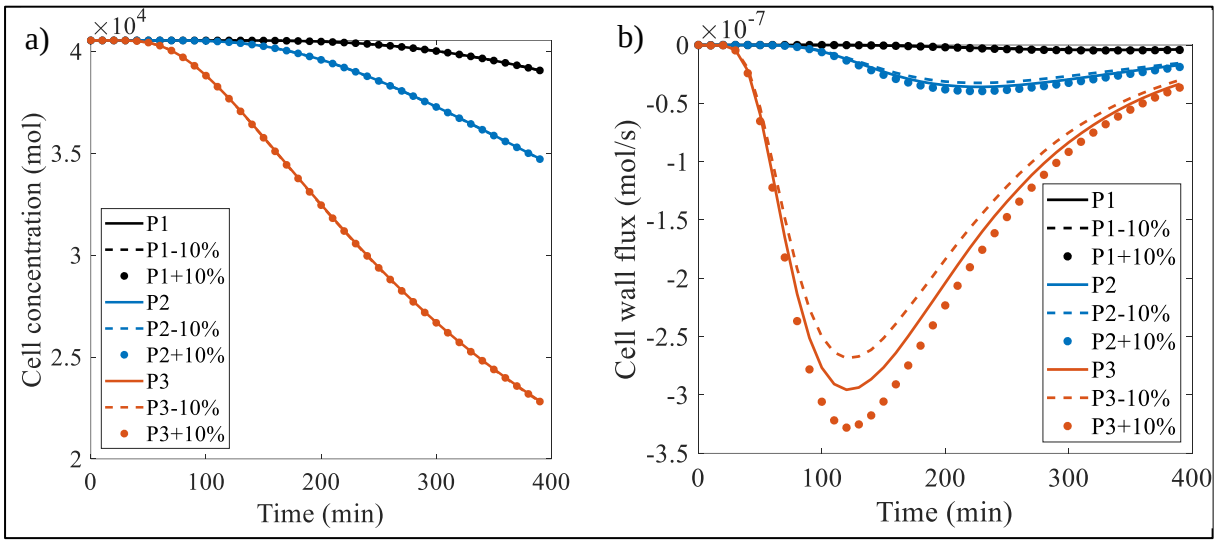

Figure C.3. Sensitivity investigation for the cell wall permeability ±10%, a) moisture concentration (mol), at each point of interest b) cell wall flux (mol/s) at each point of interest.

Appendix D - Alternative function for thermal conductivity

Multiple function exists in literature for the thermal conductivity for granny smith apple. To investigate this uncertainty two common functions were investigated, and the results can be seen in Figure D.1. The functions resulted in the same MRE for the average moisture content and temperature. The functions investigated were, $0.490-0.443\cdot\exp(-0.206\cdot M_{db})$ (Mattea et al., 1986), and $0.148+0.493\cdot M_{db}$ (SWEAT, 1974).

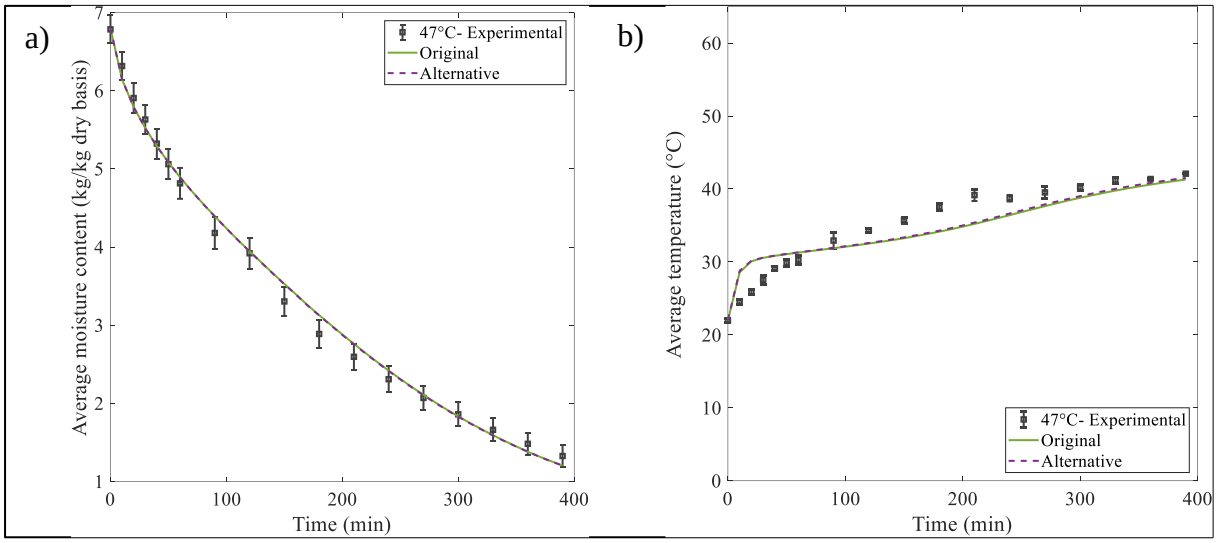

Figure D.1. Comparing different function for thermal conductivity for drying at 47°C, a) average moisture content (kg/kg dry basis) b) Average surface temperature (°C).

References

Mattea, M., Urbicain, M. J., & Rotstein, E. (1986, 1986/01/01). Prediction of Thermal Conductivity of Vegetable Foods by the Effective Medium Theory. *Journal of Food Science, 51*(1), 113-115. https://doi.org/10.1111/j.1365-2621.1986.tb10848.x

SWEAT, V. E. (1974). EXPERIMENTAL VALUES OF THERMAL CONDUCTIVITY OF SELECTED FRUITS AND VEGETABLES. *Journal of Food Science*, *39*(6), 1080-1083. https://doi.org/10.1111/j.1365-2621.1974.tb07323.x